

Transferable machine learning approach for predicting electronic structures of charged defects

Cite as: Appl. Phys. Lett. **126**, 044103 (2025); doi: [10.1063/5.0242683](https://doi.org/10.1063/5.0242683)

Submitted: 6 October 2024 · Accepted: 8 December 2024 ·

Published Online: 27 January 2025



View Online



Export Citation



CrossMark

Yuxing Ma,^{1,2} Hongyu Yu,^{1,2} Yang Zhong,^{1,2,a} Shiyou Chen,^{1,2} Xingao Gong,^{1,2} and Hongjun Xiang^{1,2,a}

AFFILIATIONS

¹Key Laboratory of Computational Physical Sciences (Ministry of Education), Institute of Computational Physical Sciences, State Key Laboratory of Surface Physics, and Department of Physics, Fudan University, Shanghai 200433, China

²Shanghai Qi Zhi Institute, Shanghai 200030, China

^aAuthors to whom correspondence should be addressed: yzhong@fudan.edu.cn and hxiang@fudan.edu.cn

ABSTRACT

The study of electronic properties of charged defects plays a crucial role in advancing our understanding of how defects influence conductivity, magnetism, and optical behavior in various materials. However, despite its significance, research on large-scale defective systems has been hindered by the high computational cost associated with density functional theory (DFT). In this study, we propose HamGNN-Q, an E(3) equivariant graph neural network framework capable of accurately predicting DFT Hamiltonian matrices for diverse point defects with varying charges, utilizing a unified set of network weights. By incorporating background charge features into the element representation, HamGNN-Q facilitates a direct mapping from structural characteristics and background charges to the electronic Hamiltonian matrix of charged defect systems, obviating the need for DFT calculations. We showcase the model's high precision and transferability by evaluating its performance on GaAs systems encompassing diverse charged defect configurations. Furthermore, we predicted the wave function distribution of polarons induced by defects. We analyzed the node features through principal component analysis, providing physical insights for the interpretability of the HamGNN-Q model. Our approach provides a practical solution for accelerating electronic structure calculations of neutral and charged defects and advancing the design of materials with tailored electronic properties.

Published under an exclusive license by AIP Publishing. <https://doi.org/10.1063/5.0242683>

The presence of charged defects introduces additional electronic states within the bandgap of semiconductors or modifies existing energy levels near the conduction and valence bands.^{1,2} This alteration in electronic structure leads to profound changes in material properties. Compared with neutral defects, introducing non-equilibrium charge states by charged defects adds a new dimension to defective systems, significantly influencing not only the electrical and optical properties but also semiconductor behavior.^{1,3–5} For instance, the introduction of charged defects can change both defect formation energies and transition energy levels, rendering them more dynamic and active compared to their neutral counterparts.⁶ This is further reflected in their ability to modulate trapping rates of electrons and holes,^{7,8} thereby affecting charge carrier transport efficiency in materials. Additionally, charged defects can influence luminescence quenching rates,⁹ which are crucial for applications such as solar cells where photoluminescence plays a pivotal role. In solar cells specifically, Coulombic scattering induced by charged defects can substantially

impact carrier transport, thus influencing overall cell efficiency. Therefore, investigation into the behavior and properties of charged defects in materials is crucial not only for understanding material performance but also for providing valuable insights into manipulating charged defects to enhance desired material properties and performance in specific applications.

Currently, the determination of electronic structures in materials heavily relies on density functional theory (DFT) calculations, which exhibit limited scalability and necessitate numerous computationally expensive self-consistent iterations to achieve converged Hamiltonian matrices. Consequently, the calculation of electronic structure for defect models containing a large number of atoms is a significant challenge for DFT methods. Furthermore, when dealing with defective systems, employing finite-sized supercells may give rise to spurious interactions between defects in neighboring supercells.^{10,11} Therefore, considering a larger unit cell becomes necessary when studying charged defects. To address this issue, semi-empirical tight-binding

(TB) approximations,¹² such as the Slater–Koster method,¹³ have been proposed. Although it can provide a reasonable approximation of electronic structures while reducing computational costs by using simplified analytical models and manual semi-empirical parameters, accurately predicting electronic structures for general systems remains challenging. These limitations hinder the investigation of material properties in large systems from the DFT level. Recently, the utilization of neural networks for parameterizing DFT Hamiltonians has garnered widespread attention and has been proven to be an effective method for accelerating electronic structure calculations.^{14–16} Although ML Hamiltonian models have achieved great success and have been widely applied in the field of perfect crystalline systems, further improvements are needed to explore and understand the complex physical behavior of defects in materials. These models need to be enhanced to incorporate charge information and enable transferability across different charge states.

In this study, we designed the HamGNN-Q model for predicting the DFT Hamiltonian of charged defect systems. The model integrates the features of background charge (Q) and element representation (Z) to effectively capture the transfer of charge information through a message-passing neural network (MPNN). After training on the Hamiltonian matrices obtained from first-principles calculations for GaAs systems, the HamGNN-Q achieves high-precision predictions across various cell sizes, defect configurations, and background charges, demonstrating excellent transferability and generalization. Leveraging the trained HamGNN-Q model, we efficiently computed the electronic properties, including band structures and charge density distributions, for large-scale defective systems with neutral and charged states. Furthermore, principal component analysis revealed a significant correlation between the atomic features and the charges they carry, indicating that the network can accurately capture the redistribution of charges. In summary, the proposed approach provides a practical solution for accelerating *ab initio*-level electronic structure calculations in complex defective materials.

We designed an E(3) equivariant HamGNN-Q model to fit the *ab initio* Hamiltonian matrix of the charged defect. HamGNN-Q can realize direct mapping from atomic species, atomic positions, and background charge Q to *ab initio* Hamiltonian matrix. As shown in Fig. 1(a), HamGNN-Q first embeds the atomic species Z_i , interatomic distances $\|\vec{r}_{ij}\|$, and relative orientations $\hat{\vec{r}}_{ij}$ in the initial feature vectors \mathbf{V}_i^0 . The interatomic distances are expanded using Bessel basis functions,

$$B(\|\vec{r}_{ij}\|) = \sqrt{\frac{2}{r_c}} \frac{\sin(n\pi\|\vec{r}_{ij}\|)}{\|\vec{r}_{ij}\|} f_c(\|\vec{r}_{ij}\|), \quad (1)$$

where f_c is the cosine cutoff function, which guarantees physical continuity for the neighbor atoms close to the cutoff sphere. The direction between atom i and atom j is embedded into a set of real spherical harmonics $Y^l(\hat{\vec{r}}_{ij})$, which are used to construct rotationally equivariant filters in equivariant message passing.

The atomic species (Z_i) and the background charge (Q) are encoded as one-hot vectors, respectively, and then transformed into the whole initial atomic features $\mathbf{V}_i^0 \oplus \mathbf{Q}_i^0$ through a multi-layer perceptron (MLP), as shown in Fig. 1(b). Here, Q_i is initialized by background charge (Q). The node convolution layers are utilized to construct equivariant messages by aggregating the features of the

neighbor atoms within a cutoff radius. The architecture of the node convolution layer is presented in Fig. 1(c). In the construction of the equivariant message $\mathbf{m}_i^{t,l}$, atomic species and charge features are combined with the features of its neighboring atoms,

$$\mathbf{m}_i^{t,l} = \sum_{j \in N(i)} M_j^{t,l} \left(\mathbf{V}_i^{t,l} \oplus \mathbf{Q}_i^{t,l}, \mathbf{V}_j^{t,l} \oplus \mathbf{Q}_j^{t,l}, \vec{r}_{ij} \right), \quad (2)$$

$$M_j^{t,l} = \text{MLP}(B(\|\vec{r}_{ij}\|)) \left[\mathbf{W}_j^l \left(\mathbf{V}_j^{t,l} \oplus \mathbf{Q}_j^{t,l} \right) \right] \otimes Y^l(\hat{\vec{r}}_{ij}), \quad (3)$$

where $M_j^{t,l}$ is the message function, $\mathbf{V}_i^{t,l}$ and $\mathbf{Q}_i^{t,l}$, respectively, denotes the features of the element and charge features of atom i in the node convolution layer t ($t \leq T$), l ($l \leq l_{\max}$) is the rotation order of the O(3) irreducible representation, and \mathbf{W}_j^l denotes a learnable weight matrix for the l th order equivariant features. The message $\mathbf{m}_i^{t,l}$ is required to be equivariant and is constructed through spherical harmonics function. In addition, the features are scaled by an invariant scalar derived from the distance between atoms, and these scalar features are subsequently employed as weights in the equivariant output process.

In each node convolution layer, the charge information is passed through a message-passing neural network (MPNN), as presented in Fig. 1(d). The node features are updated with the received equivariant messages from the neighbors as follows:

$$\mathbf{V}_i^{t+1,l} \oplus \mathbf{Q}_i^{t+1,l} = \mathbf{W}_i^l \left(\mathbf{V}_i^{t,l} \oplus \mathbf{Q}_i^{t,l} \right) + \sum_{j \in N(i)} \mathbf{m}_j^{t,l}. \quad (4)$$

With the iteration of multiple convolution layers, more and more atomic information will be aggregated into the features, thereby realizing the update of node features.

The pair interaction features, which are utilized to construct Hamiltonian matrices, are constructed in the pair interaction layer by taking the tensor product of the linearly mixed features of atom pair ij with the convolution filter,

$$\mathbf{P}_{ij}^{l,q} = \text{MLP}^l(\|\vec{r}_{ij}\|) \left[\mathbf{W}_{ij}^l \left(\mathbf{V}_i^{T,l} \oplus \mathbf{Q}_i^{T,l} \| \mathbf{V}_j^{T,l} \oplus \mathbf{Q}_j^{T,l} \right) \right] \otimes Y^l(\hat{\vec{r}}_{ij}). \quad (5)$$

According to Wigner–Eckart theorem, the reducible spherical tensor can be converted to the direct sum of several irreducible spherical tensors (ISTs) as follows:

$$l_i \otimes l_j = |l_i - l_j| \oplus |l_i - l_j| + 1 \oplus \cdots \oplus |l_i + l_j|, \quad (6)$$

where $l_i \otimes l_j$ is a reducible representation. Therefore, each sub-block of the Hamiltonian matrix (l_i, l_j) can be equivalently represented as a direct sum of ISTs in accordance with Eq. (7).

The Hamiltonian output block utilizes the node features $\mathbf{V}_i^{T,l} \oplus \mathbf{Q}_i^{T,l}$ and pair interaction features $\mathbf{P}_{ij}^{l,q}$ to construct sub-blocks of on-site and off-site Hamiltonian matrices, respectively. This is achieved by employing the following equation:

$$H_{l_i m_i, l_j m_j} = \sum_{l=|l_i - l_j|}^{l_i + l_j} \sum_{m=-l}^l C_{m_i, m_j, m}^{l_i, l_j, l} \mathbf{X}_{l, m}^{l_i, l_j} \quad (\mathbf{X} = \mathbf{V}_i \oplus \mathbf{Q}_i \text{ or } \mathbf{V}_{ij} \oplus \mathbf{Q}_{ij}), \quad (7)$$

where $C_{m_i, m_j, m}^{l_i, l_j, l}$ denotes Clebsch–Gordan coefficients, $\mathbf{V}_i \oplus \mathbf{Q}_i$ represents the node feature, and $\mathbf{V}_{ij} \oplus \mathbf{Q}_{ij}$ represents the edge feature of nodes i and j .

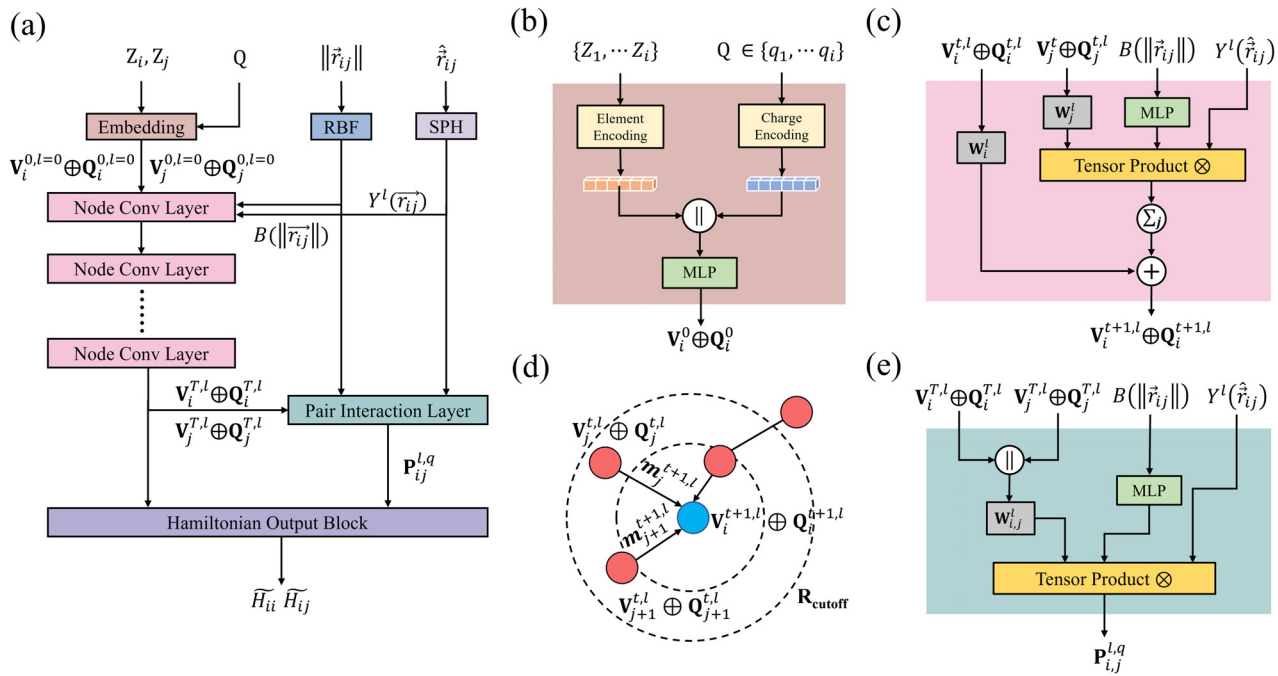


FIG. 1. (a) The overall network architecture of HamGNN-Q: An initial graph of element species, background charge, interatomic distances, and interatomic directions of the crystal are embedded into the input tensor. The atomic orbital features with angular momentum l are included in the l -order components of the $O(3)$ equivariant tensors and are updated through T convolution layers. The pair interaction features $P_{ij}^{l,q}$ and node features are integrated to construct the Hamiltonian matrices through Hamiltonian output block. (b) Schematic diagram of background charge embedding: Charge information and element species are embedded into the node features by one-hot encoding. (c) Node conv layer: The equivariant features of atomic orbitals are refined by the message functions and update functions. (d) Illustration of the charge information message-passing (MP) process: The node features and edge features are updated via message functions $m_j^{t,l}$ from neighboring nodes within the cutoff radius (R_{cutoff}). (e) Pair interaction layer: This layer is utilized to construct pair interaction features between adjacent atomic orbitals through equivariant tensor products.

01 February 2025 08:44:28

When the training of the model is not converged, the prediction accuracy of the Hamiltonian will be low, resulting in inaccurate band energy obtained through diagonalization of the Hamiltonian in reciprocal space. To address this issue, we propose a training method that introduces a regularization error term for computing band energy loss into the total loss function,

$$L = \|\tilde{H} - H\| + \frac{\lambda}{N_{\text{pick}} \times N_k} \sum_{k=1}^{N_k} \sum_{n=1}^{N_{\text{pick}}} \|\tilde{\epsilon}_{nk} - \epsilon_{nk}\|, \quad (8)$$

where L represents the total loss function, H and ϵ_{nk} represent the Hamiltonian and band energy, respectively, the variables marked with a tilde refer to the corresponding predictions, λ represents the loss weight of band energy error, N_k represents the number of randomly selected k points in the Brillouin zone where the Hamiltonian is diagonalized, and N_{pick} represents the number of bands picked near the Fermi level. Incorporating a band error term into the loss function can improve the transferability of the model trained in the first round.

Based on the above, the training of HamGNN-Q is divided into two steps. First, only the mean absolute error (MAE) of the Hamiltonian matrix is used as the loss value to train the network and the initial learning rate is set to 0.01. When the network reaches a loss value of 10^{-4} , the MAE of each band energy calculated at random k points in the reciprocal space is added to the total loss function. The learning rate is readjusted to 10^{-4} , and training is restarted until the

network weights are completely converged. Compared with directly training the Hamiltonian, this training process improves training efficiency and prevents overfitting by simultaneously fitting both the real-space Hamiltonian and the band energy of the reciprocal Hamiltonian.

The GaAs system with charged defects was chosen to verify the performance of HamGNN-Q. GaAs demonstrates exceptional optoelectronic properties and semiconductor behavior, making it highly versatile for applications in optoelectronic devices, including solar cells, detectors, and LEDs.^{17–19} However, during the fabrication process of GaAs, numerous charged defects, such as vacancies, impurities, and dislocations, can potentially arise, exerting significant influences on the performance of GaAs semiconductor materials.^{20–22} Therefore, the electronic properties of charged defect systems in GaAs necessitate thorough research.

We calculated the real-space Hamiltonian matrices using OpenMX^{23,24} for approximately 4600 structures derived from high-temperature molecular dynamics trajectories. The entire dataset was divided into the training set, test set, and verification set with a ratio of 0.8:0.1:0.1. Within the dataset, various amounts of background charge and different types of defect, including vacancy, interstitial atom defect, and defect clusters formed by their combination, were considered. Further details regarding the dataset can be found in the [supplementary material](#).

As shown in Fig. 2(a), the predicted Hamiltonian matrix exhibits excellent agreement with the calculation by DFT. The trained

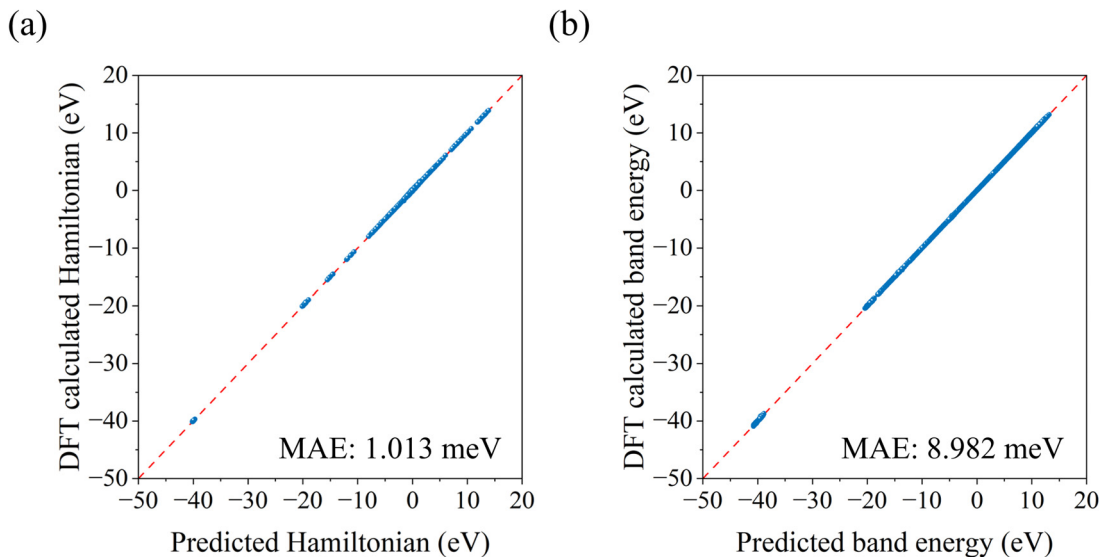


FIG. 2. (a) Comparison of the HamGNN-Q predicted Hamiltonian matrix elements with the OpenMX calculated Hamiltonian matrix elements on the test set. (b) Comparison of predicted and calculated band energy on the test set.

HamGNN-Q model achieves an MAE of 1.013 meV for the Hamiltonian matrix elements on the test set. Furthermore, as depicted in Fig. 2(b), the predicted Hamiltonian reproduces the energy levels obtained from DFT calculations, indicating the high accuracy in predicting the band structure via the model.

In practical scenarios, multiple types of defects often coexist in materials. To test the performance of HamGNN-Q, we constructed different combinations of vacancy and interstitial defects for testing. As shown in Figs. 3(a) and 3(b), we constructed an As double-vacancy defect (DV_{As-As}^{6-}) and a Ga double interstitial defect (DI_{Ga-Ga}^{6+}), and the amount of background charge for them is -6 and $+6$, respectively. By using the predicted Hamiltonian via HamGNN-Q, we can obtain the band structures that almost exactly agree with the DFT calculations. Moreover, we also investigated the coexistence of different defect types. As shown in Fig. 3(c), we constructed a combination of a vacant As and an interstitial Ga with a background charge of $6 [I_{Ga} - V_{As}]^{6+}$. By employing the predicted Hamiltonian, we calculated the corresponding band structures. The obtained results exhibit good agreement with the DFT calculations, further validating the accuracy of our model. In addition to the aforementioned cases, we also test the transferability of HamGNN-Q. We constructed substitutional defects that totally do not exist in our training set. As shown in Figs. 3(d) and 3(e), we considered structures of a single As substituted by Ga (Ga_{As}^{6+}) and a single Ga substituted by As (As_{Ga}^{6-}), and the amount of background charge for them is $+6$ and -6 , respectively. It can be seen that the calculated band structures from HamGNN-Q match the DFT results well. Subsequently, more complex defect interactions were considered, and we constructed a substitutional defect cluster at the nearest neighbor atomic positions, as depicted in Fig. 3(f). The atomic position originally designated for Ga was replaced with As, while the atomic position intended for As was substituted with Ga. Observably, the band structures derived from the Hamiltonian predicted from HamGNN-Q display a notable concordance with the DFT results. From the side,

HamGNN-Q demonstrates exceptional generalization capability, providing reliable predictions even for structures that were not included in the training set.

Utilizing the trained HamGNN-Q model, we computed the band structures and corresponding charge density distributions of As vacancy defects under various charge states and defect concentrations. The As vacancy defect was chosen for the computational model due to its lower formation energy, making it more likely to occur during material growth.

As illustrated in Fig. 4(a), an As single-vacancy defect without any additional net charge is in a $2 \times 2 \times 2$ supercell, and its defect concentration is 1.56 at. %. It can be seen from the band structure [Fig. 4(d)] predicted by HamGNN-Q that the bottom of the conduction band produces impurity energy levels (marked by the red solid line) due to vacancy. From the corresponding charge density distribution [Fig. 4(g)], it can be seen that the charges are mainly concentrated near the vacancy defects. Here, for comparison with other results, the charge density map was scaled up by a factor of two. Charge accumulation still occurs at positions far from the vacancy and near the lattice boundaries. This phenomenon is attributed to the higher defect concentration caused by the use of a small simulation cell and periodic boundary conditions (PBCs), which amplify interactions between defects and influence the charge density distribution. Similarly, an identical atomic structure is considered, with a net charge of $+3$, as shown in Fig. 4(b). It also can be observed from the band structure plot that there are still shallow energy levels caused by vacancy defects [Fig. 4(e)]. Furthermore, the introduction of additional net charges induces slight changes in the shape of the band structure. In contrast to Fig. 4(g), the charge density distribution with a net charge appears more delocalized, potentially due to the influence of Coulombic interactions. Subsequently, we examined a $4 \times 4 \times 4$ supercell carrying a net charge of $+3$, and its defect concentration is 0.20 at. % [Fig. 4(c)]. As shown in Fig. 4(f), the band structure predicted by HamGNN-Q

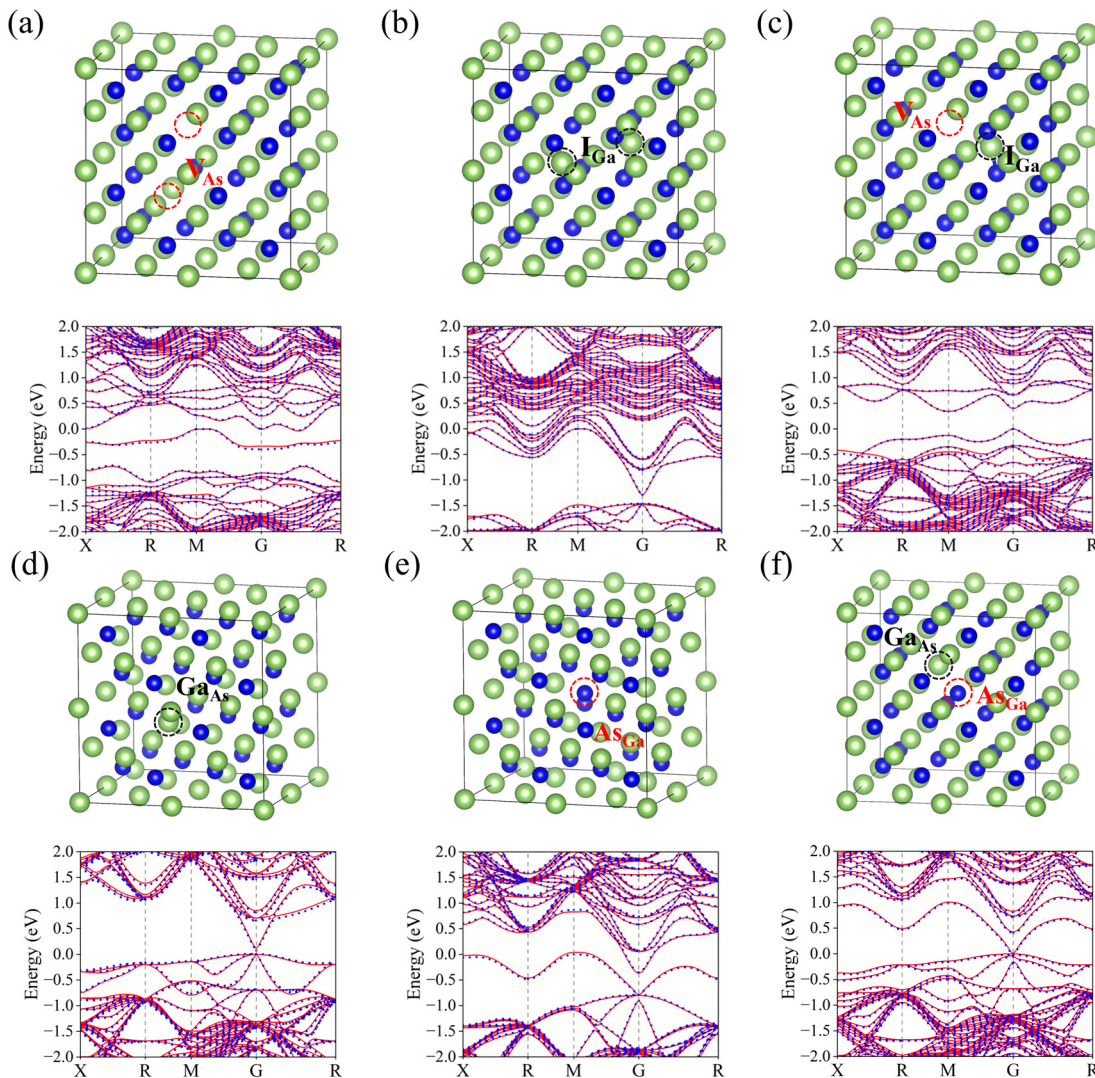


FIG. 3. (a) Crystal structure of an As double-vacancy defect with a background charge of -6 (DV_{As-As}^{6-}) and its band structure. The blue balls represent As atoms, and the green balls represent Ga atoms. The red dotted circle indicates vacant As atoms. (b) Crystal structures of a Ga double interstitial defect with a background charge of 6 (D_{Ga-Ga}^{6+}) and its band structure. The dark dotted circle indicates interstitial Ga atoms. (c) The crystal structure of a defect cluster comprises a vacant As and an interstitial Ga with a background charge of 6 [$I_{Ga} - V_{As}^{6+}$] and its band structure. The red dotted circle and the dark dotted indicate a vacant As atom and an interstitial Ga atom, respectively. (d) Crystal structure of As substituted by Ga (Ga_{As}^{6+}) and its band structure. The dark dotted circle indicates the Ga atom after replacing As. (e) Crystal structure of As substituted by Ga (As_{Ga}^{6+}) and its band structure. The red dotted circle indicates the As atom after replacing Ga. (f) Crystal structure of a substitution defect cluster at the nearest neighbor atomic positions with a background charge of 0 [$As_{Ga} - Ga_{As}]^0$ and its band structure. The red dot circle and dark dot represent the substitution defect of Ga atoms by As and the substitution defect of As atoms by Ga, respectively. All the above band structure computed by HamGNN-Q (red solid line) and DFT calculation (blue short dot), respectively.

illustrates that, with decreasing defect concentration. The bands of shallow energy levels are folded and gradually transition into flat bands. From the charge density distribution of the big-size cell as shown in Fig. 4(i), it can be observed that the charge accumulates near the vacancy and exhibits high localization. Therefore, the defect concentration significantly influences the charge density distribution at the defect site. Larger cells, corresponding to lower defect concentrations, exhibit a more localized charge distribution compared to smaller cells. Our results indicate that both the background charge and defect

concentration affect the shape of the band structure and the charge density distribution in the defect system.

Polarons, as a fundamental manifestation of electron-lattice interactions, have garnered significant attention in the past decade.^{25–27} However, previous studies have predominantly relied on idealized mathematical models. While these models provide valuable insights into the fundamental characteristics of polarons, they neglect the material structure at the atomic scale. Furthermore, DFT faces challenges such as demanding computational resources and the need for large

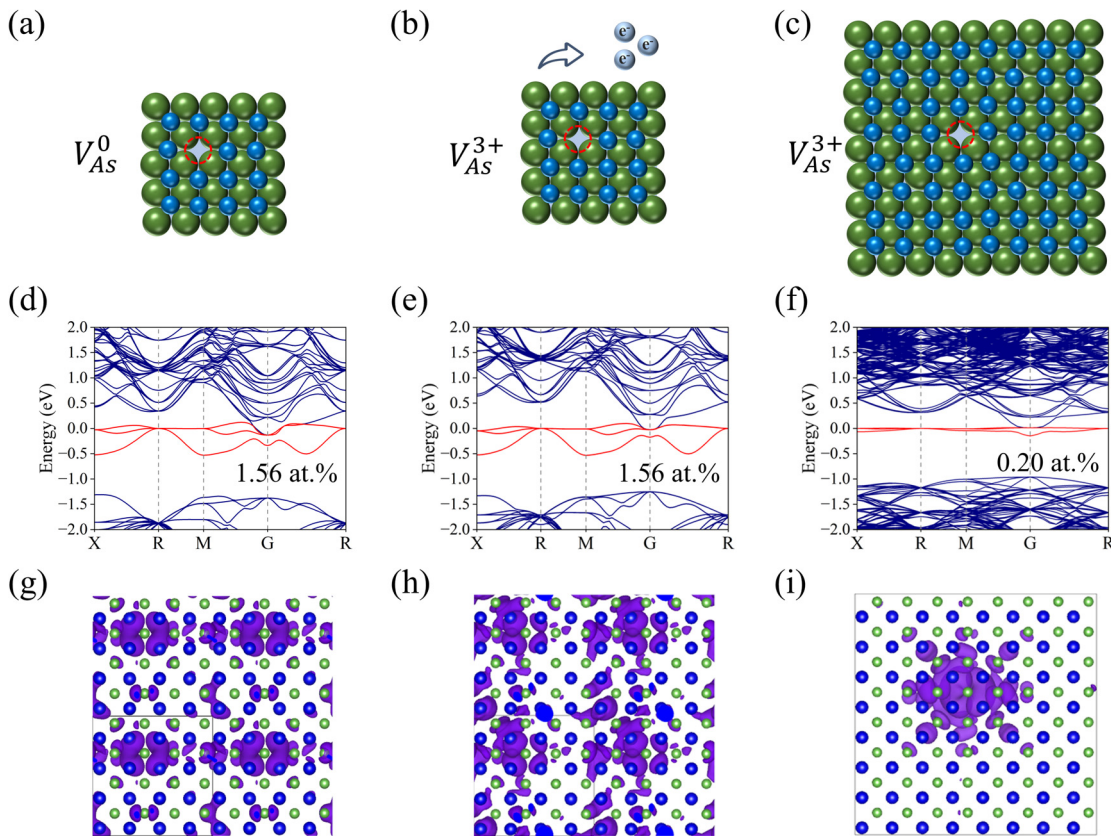


FIG. 4. (a) The As vacancy defect (V_{As}^0) with a neutral charge state and a defect concentration of 1.56 at %. (b) The As vacancy defect (V_{As}^{3+}) with a net charge of +3 at a defect concentration of 1.56 at %. (c) The As vacancy defect (V_{As}^{3+}) with a net charge of +3 at a defect concentration of 0.20 at %. (d)–(f) The band structures corresponding to (a), (b), and (c), respectively. The red lines correspond to the defect levels near the bottom of the conduction band. (g)–(i) The charge density distribution corresponding to (a), (b), and (c), respectively.

01 February 2025 08:44:28

supercells when dealing with complex systems. Despite the efficiency improvements offered by perturbation theories, our trained HamGNN-Q model demonstrates faster computational capabilities and the ability to handle large-scale systems.

A large-scale substitutional charged defect system comprising 13824 atoms was constructed, where an As atom replaces a Ga atom with a net charge of 6 (As_{Ga}^{6+}). As shown in Fig. 5(a), the shallow energy levels introduced by the defect appear, which significantly narrows the bandgap of bulk GaAs. The charge density distribution at the gamma point at the bottom of the conduction band is shown in Fig. 5(b), the predicted charge density distribution by HamGNN indicates the formation of polarons due to the introduction of substitution defects. The charge distribution is mainly concentrated around the substituted atoms, and the polaron range is large, with a diameter of about 40 Å. Therefore, HamGNN-Q accelerates the process of studying polarons on an *ab initio* level, providing a fast and accurate tool for calculating the electron-related properties of polarons.

As widely acknowledged in deep learning, models constructed by intricate network structures and a multitude of parameters often present challenges in the interpretability of their prediction outcomes. To facilitate a more profound understanding of the prediction outcomes,

there is a need to enhance the interpretability of HamGNN-Q. We utilize the principal component analysis (PCA) approach to reduce the dimensionality of the node features of the As_{Ga} defect with net charges, compressing them into a more visually accessible three-dimensional representation. The outcomes of the PCA are shown via a scatterplot in Fig. 5(c). It can be seen that there is an evident clustering, with the majority of data points converging toward the center of the figure. Furthermore, there are still a few small clusters distributed around the central area. To further investigate the details of results from PCA, we divide all principal component (PC) points obtained via dimensionality reduction into two categories: one type is located at the cluster center (Ga, As) and the other type is located far away from the cluster center (Ga outliers, As outliers). We displayed these two categories of PC points and their corresponding elements in the atomic structure diagram. As shown in Fig. 5(d), points situated far from the clustering center correspond to atoms located in the vicinity of As_{Ga} substitution defects. However, the points located at the center of the cluster account for the majority and they are far away from the defect location. The points close to the cluster center represent electrical neutrality and their node features exhibit similarities. It can be seen that HamGNN-Q captures the charge feature of atoms in different charge states in charged defects. From the outcomes of PCA, we can see that based on

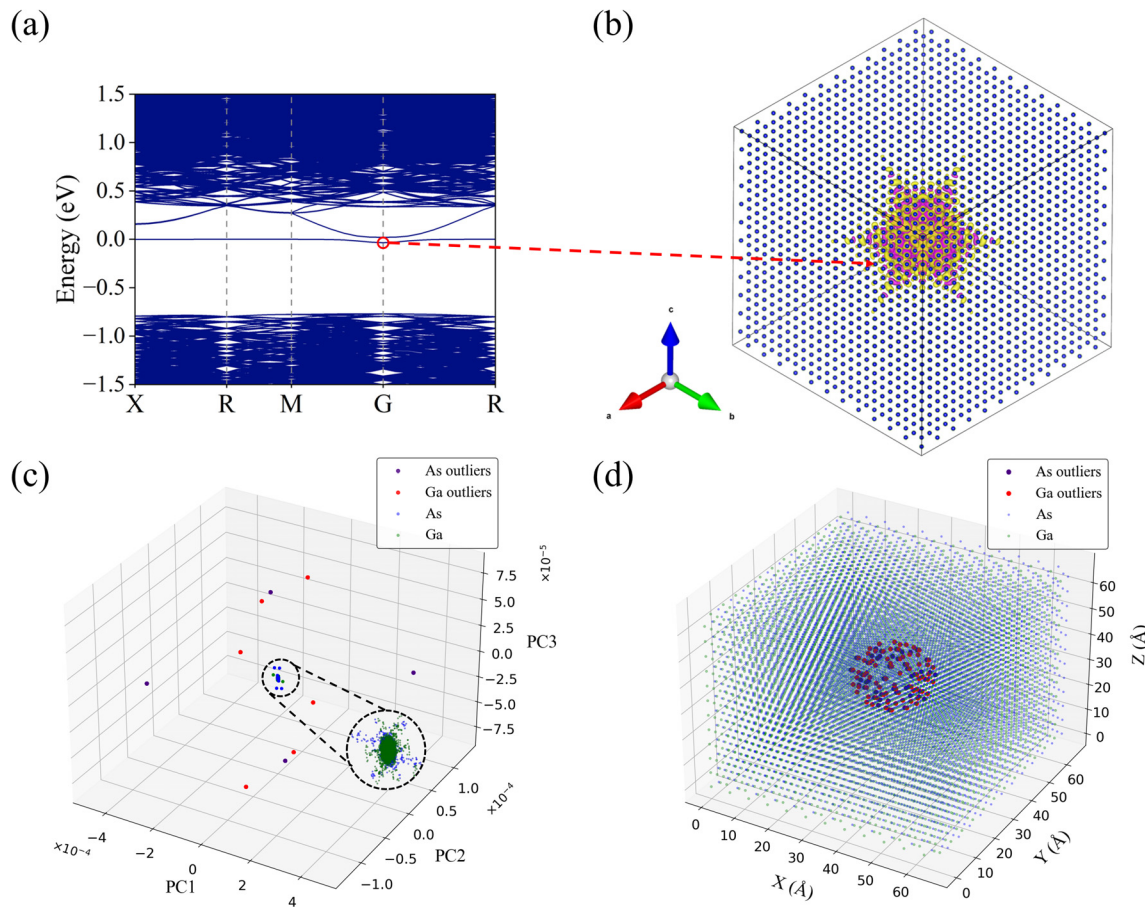


FIG. 5. Schematic diagram of polarons generated by As_{Ga} substitution defects. (a) Wave function distribution of the polaron. (b) The energy bands of As_{Ga} substitution defect. (c) Principal component analysis (PCA) plot for node feature of As_{Ga} defect. After PCA is applied to this atomic structure, the projections of node features are plotted along their three principal components (PCs). (d) Schematic diagram of atomic distribution corresponding to PCA clustering results.

multiple iterations of MPNN, HamGNN-Q can fit the atomic node feature and charged defect state feature, and then accurately predict the Hamiltonian of the charged defect system. This proves the effectiveness of our method and enhances the model's interpretability and physical meaning.

In this study, we propose a HamGNN-Q graph neural network that exhibits $E(3)$ equivariance for predicting the DFT Hamiltonian. This network enables us to fit the Hamiltonian of charged defect systems by incorporating background charge information into the graph representation. For charged defect systems in GaAs, our model establishes a direct mapping from the atomic structure and charge information to the DFT Hamiltonian without the need for computationally expensive self-consistent field (SCF) iterations. HamGNN-Q demonstrates a robust capability to predict the Hamiltonian of single-point defects and diverse defect clusters with varying charge states. Furthermore, the model exhibits transferability, allowing it to predict structures that are not present in the training dataset. We calculated the band structure and charge density distribution of arsenic vacancy defects at various defect concentrations. The results indicate that both the size of the

simulation cell and the quantity of charge significantly influence the charge density distributions of the defect states. For single arsenic vacancies, the charges distributed around the defect are more localized in larger cells. Additionally, we explored the charge distribution of polarons induced by defects containing more than 13,000 atoms, and the results show that HamGNN-Q provides an effective method for studying polarons in large simulation cells. Importantly, we employ the principal component analysis (PCA) method to quantitatively analyze the node features, revealing the physical meaning of our models. Therefore, our HamGNN-Q model offers a promising approach for investigating the electronic structure of large-scale charged defects and polarons.

See the [supplementary material](#) for detailed method sections and additional discussion, which include the Hamiltonian datasets, details on DFT calculations, the error of machine learning interatomic potential (MLIP), tests on the energy band for different structures and background charges, tests in TiO_2 defect system using HSE hybrid-functional method, and discussion of prediction efficiency for HamGNN-Q.

We acknowledge the financial support of the Ministry of Science and Technology of the People's Republic of China (No. 2022YFA1402901), NSFC (Grant Nos. 11825403, 11991061, and 12188101), and the Guangdong Major Project of the Basic and Applied Basic Research (Future functional materials under extreme conditions–2021B0301030005).

AUTHOR DECLARATIONS

Conflict of Interest

The authors have no conflicts to disclose.

Author Contributions

Yuxing Ma and **Yang Zhong** contributed equally to this work.

Yuxing Ma: Conceptualization (equal); Data curation (equal); Formal analysis (equal); Investigation (equal); Methodology (equal); Project administration (equal); Resources (equal); Software (equal); Writing – original draft (equal). **Hongyu Yu:** Validation (supporting). **Yang Zhong:** Conceptualization (equal); Data curation (equal); Formal analysis (equal); Investigation (equal); Methodology (equal); Project administration (equal); Resources (equal); Software (equal). **Shiyou Chen:** Writing – review & editing (supporting). **Xin-gao Gong:** Writing – review & editing (supporting). **Hongjun Xiang:** Conceptualization (equal); Writing – review & editing (equal).

DATA AVAILABILITY

The data that support the findings of this study are openly available in HamGNN at <https://github.com/QuantumLab-ZY/HamGNN>, Ref. 28 and Zenodo at <https://zenodo.org/records/11171478>, Ref. 29.

REFERENCES

- ¹E. G. Seebauer and M. C. Kratzer, "Charged point defects in semiconductors," *Mater. Sci. Eng., R Rep.* **55**(3–6), 57–149 (2006).
- ²A. M. Ganose, D. O. Scanlon, A. Walsh, and R. L. Z. Hoye, "The defect challenge of wide-bandgap semiconductors for photovoltaics and beyond," *Nat. Commun.* **13**(1), 4715 (2022).
- ³M. Y. Toriyama, M. K. Brod, and G. J. Snyder, "Chemical interpretation of charged point defects in semi-conductors: A case study of Mg₂Si," *ChemNanoMat* **8**(9), e202200222 (2022).
- ⁴B. A. Gregg, "Charged defects in soft semiconductors and their influence on organic photovoltaics," *Soft Matter* **5**(16), 2985 (2009).
- ⁵F. J. Stützler and H. J. Queisser, "Charged defect states at silicon grain boundaries," *J. Appl. Phys.* **60**(11), 3910–3915 (1986).
- ⁶S. J. Clark, J. Robertson, S. Lany, and A. Zunger, "Intrinsic defects in ZnO calculated by screened exchange and hybrid density functionals," *Phys. Rev. B* **81**(11), 115311 (2010).
- ⁷M. J. Puska, C. Corbel, and R. M. Nieminen, "Positron trapping in semiconductors," *Phys. Rev. B* **41**(14), 9980–9993 (1990).
- ⁸P. Mascher, S. Dannefaer, and D. Kerr, "Positron trapping rates and their temperature dependencies in electron-irradiated silicon," *Phys. Rev. B* **40**(17), 11764–11771 (1989).
- ⁹J. M. Ball and A. Petrozza, "Defects in perovskite-halides and their effects in solar cells," *Nat. Energy* **1**(11), 16149 (2016).
- ¹⁰G. Makov and M. C. Payne, "Periodic boundary conditions in *ab initio* calculations," *Phys. Rev. B* **51**(7), 4014–4022 (1995).
- ¹¹J. Neugebauer and M. Scheffler, "Adsorbate-substrate and adsorbate-adsorbate interactions of Na and K adlayers on Al(111)," *Phys. Rev. B* **46**(24), 16067–16080 (1992).
- ¹²C. M. Goringe, D. R. Bowler, and E. Hernández, "Tight-binding modelling of materials," *Rep. Prog. Phys.* **60**(12), 1447–1512 (1997).
- ¹³D. A. Papaconstantopoulos and M. J. Mehl, "The Slater Koster tight-binding method: A computationally efficient and accurate approach," *J. Phys.* **15**(10), R413–R440 (2003).
- ¹⁴H. Li, Z. Wang, N. Zou, M. Ye, R. Xu, X. Gong, W. Duan, and Y. Xu, "Deep-learning density functional theory Hamiltonian for efficient *ab initio* electronic-structure calculation," *Nat. Comput. Sci.* **2**(6), 367–377 (2022).
- ¹⁵X. Gong, H. Li, N. Zou, R. Xu, W. Duan, and Y. Xu, "General framework for E(3)-equivariant neural network representation of density functional theory Hamiltonian," *Nat. Commun.* **14**(1), 2848 (2023).
- ¹⁶Y. Zhong, H. Yu, M. Su, X. Gong, and H. Xiang, "Transferable equivariant graph neural networks for the Hamiltonians of molecules and solids," *npj Comput. Mater.* **9**(1), 182 (2023).
- ¹⁷N. Papež, R. Dallaev, Š. Tálu, and J. Kaštýl, "Overview of the current state of gallium arsenide-based solar cells," *Materials* **14**(11), 3075 (2021).
- ¹⁸S. Derenzo, E. Bourret, S. Hanrahan, and G. Bizarri, "Cryogenic scintillation properties of n -type GaAs for the direct detection of MeV/c² dark matter," *J. Appl. Phys.* **123**(11), 114501 (2018).
- ¹⁹J. Yin, D. B. Migas, M. Panahandeh-Fard, S. Chen, Z. Wang, P. Lova, and C. Soci, "Charge redistribution at GaAs/P3HT heterointerfaces with different surface polarity," *J. Phys. Chem. Lett.* **4**(19), 3303–3309 (2013).
- ²⁰M. Yamaguchi, A. Yamamoto, and Y. Itoh, "Effect of dislocations on the efficiency of thin-film GaAs solar cells on Si substrates," *J. Appl. Phys.* **59**(5), 1751–1753 (1986).
- ²¹S. Y. Chiang and G. L. Pearson, "Properties of vacancy defects in GaAs single crystals," *J. Appl. Phys.* **46**(7), 2986–2991 (1975).
- ²²D. Pons and J. C. Bourgois, "Irradiation-induced defects in GaAs," *J. Phys. C* **18**(20), 3839–3871 (1985).
- ²³T. Ozaki and H. Kino, "Numerical atomic basis orbitals from H to Kr," *Phys. Rev. B* **69**(19), 195113 (2004).
- ²⁴T. Ozaki, "Variationally optimized atomic orbitals for large-scale electronic structures," *Phys. Rev. B* **67**(15), 155108 (2003).
- ²⁵W. H. Sio and F. Giustino, "Polarons in two-dimensional atomic crystals," *Nat. Phys.* **19**(5), 629–636 (2023).
- ²⁶Z. Ren, Z. Shi, H. Feng, Z. Xu, and W. Hao, "Recent progresses of polarons: Fundamentals and roles in photocatalysis and photoelectrocatalysis," *Adv. Sci.* **11**, 2305139 (2024).
- ²⁷C. Franchini, M. Reticcioli, M. Setvin, and U. Diebold, "Polarons in materials," *Nat. Rev. Mater.* **6**(7), 560–586 (2021).
- ²⁸See <https://github.com/QuantumLab-ZY/HamGNN> for "HamGNN."
- ²⁹Y. Ma (2024). "The energy bands of charged defect predicted by the HamGNN-Q model," Zenodo. Dataset <https://zenodo.org/records/11171478>

Supplemental Material

Transferable Machine Learning Approach for Predicting Electronic Structures of Charged Defects

Yuxing Ma^{1,2}, Hongyu Yu^{1,2}, Yang Zhong^{1,2*}, Shiyou Chen^{1,2}, Xingao Gong^{1,2},
Hongjun Xiang^{1,2*}

¹*Key Laboratory of Computational Physical Sciences (Ministry of Education), Institute of Computational Physical Sciences, State Key Laboratory of Surface Physics, and Department of Physics, Fudan University, Shanghai, 200433, China*

²*Shanghai Qi Zhi Institute, Shanghai, 200030, China*

Corresponding authors: yzhong@fudan.edu.cn and hxiang@fudan.edu.cn

Methods

Hamiltonian datasets and the DFT calculation

We generated random structural configurations of $2 \times 2 \times 2$ GaAs supercells by ab initio MD calculations using the Vienna ab initio simulation package (VASP)¹. Simulations were performed with the projector-augmented wave^{2,3} pseudopotentials and the GGA parameterized by Perdew-Berke-Ernzerhof (PBE)⁴. The cutoff energy of the plane waves was 550 eV and only the Γ point was used in our k-mesh. We generated random atomic structures of supercells by ab initio MD calculations performed at temperatures ranging from 300K to 1600K with a time step of 1 fs.

We calculated DFT Hamiltonians by OpenMX software⁵ using numerical atomic orbitals (NAO) and PBE type exchange-correlation functions. For the GaAs system, the pseudo-atomic orbitals Ga7.0-s3p2d2 and As7.0-s3p2d2 were used. The energy cutoff was set to 300 Ry. Supercell calculations were performed for a $2 \times 2 \times 2$ with 64 atoms using a $3 \times 3 \times 3$ Monkhorst–Pack k grid.

Machine learning interatomic potential (MLIP)

A machine learning potential we used based on the Allegro E(3)-equivariant machine-learning interatomic potential (MLIP) framework⁶, used to optimize large-scale atomic structures. The forces and energies accuracy of MLIP are shown in Table S3. We use

the Atomic Simulation Environment (ASE) package⁷ as the interface and adopt the fast inertial relaxation engine (FIRE) method for structural optimization. The convergence criterion is that the force on all individual atoms should be less than 0.01 eV/ Å.

Details on training the neural network.

The entire machine learning framework was implemented with Python3 scripts by using the open-source PyTorch⁸, Pymatgen⁹, Nequip, and e3nn¹⁰ libraries. The HamGNN-Q model was trained on Nvidia A100 and Nvidia A800 GPUs, the batch size was set to 1, and the initial learning rate was set to 0.001. When the accuracy of the model on the validation set remains unchanged for n consecutive epochs, the learning rate will be reduced by a factor of 0.5. If the learning rate is lower than 10^{-6} , the training will be stopped and the model that has the best accuracy on the validation set will be used on the test set.

The details of the dataset

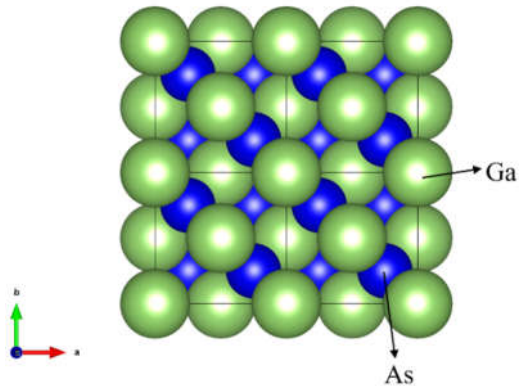


Fig.S1 Schematic diagram of the $2\times2\times2$ supercell GaAs in the HamGNN-Q training set.

In dataset preparation, we used a $2\times2\times2$ supercell configuration as the base structure. Perfect crystals and single atomic defects are considered, including vacancy defects and interstitial defects. Additionally, we accounted for three distinct background charges (+3, 0, and -3), based on the valence states of Ga and As in the GaAs system. More details are shown in Table S1. The suboptimal performance of certain structures was observed when using HamGNN-Q trained on a single-point defect dataset to

predict defect clusters that do not exist in the training set. We attribute this to the interactions between individual defects within the defect clusters, which were not present in the training set. Thus, HamGNN-Q has not learned the features of interactions. To solve this, we expanded our original dataset by adding additional data related to defect clusters; further specifics are provided in Table S2.

Table.S1 The single-atom point defect types in the training set of GaAs (2700 samples).

Defect	Perfect	V _{As}	V _{Ga}	I _{As}	I _{Ga}
Charge (q)	-3,0,3	-3,0,3	-3,0,3	-3,0,3	-3,0,3

Table S2 The defect cluster types in the training set of GaAs (1900 samples).

Defect-1 Charge	V _{As}	V _{Ga}	I _{As}	I _{Ga}
V _{As}	-6,0,6	-6,0,6	-6,0,6	-6,0,6
V _{Ga}	-6,0,6	-6,0,6	-6,0,6	-6,0,6
I _{As}	-6,0,6	-6,0,6	-6,0,6	-6,0,6
I _{Ga}	-6,0,6	-6,0,6	-6,0,6	-6,0,6

Table.S3 The accuracy of the machine learning potential of the GaAs system.

Evaluation metric	Accuracy
MAE of Force (meV/ Å)	0.524
RMSE of Force (meV/ Å)	0.673
MAE of Energy/N (meV)	0.083
RMSE of Energy/N (meV)	0.104

* Energy/N indicates the accuracy of the average energy per atom.

* MAE and RMSE represent mean absolute error and root mean squared error, respectively.

Testing for the band structure of single-point defects with different net charges

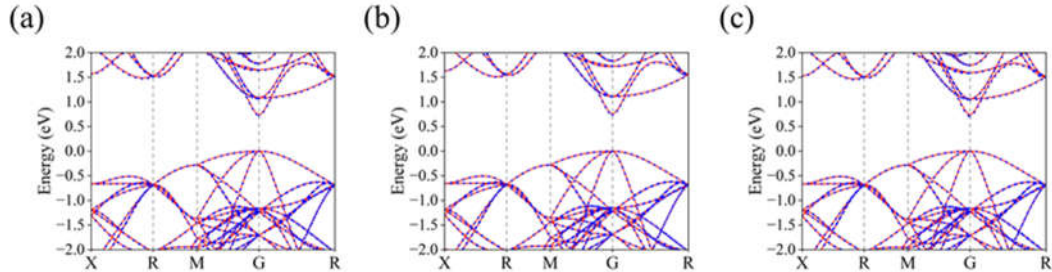


Fig.S2 The band structure for the perfect crystal of GaAs computed by HamGNN-Q (red solid line) and DFT calculation (blue dotted line). (a) Perf⁰ (b) Perf³⁺ (c) Perf³⁻.

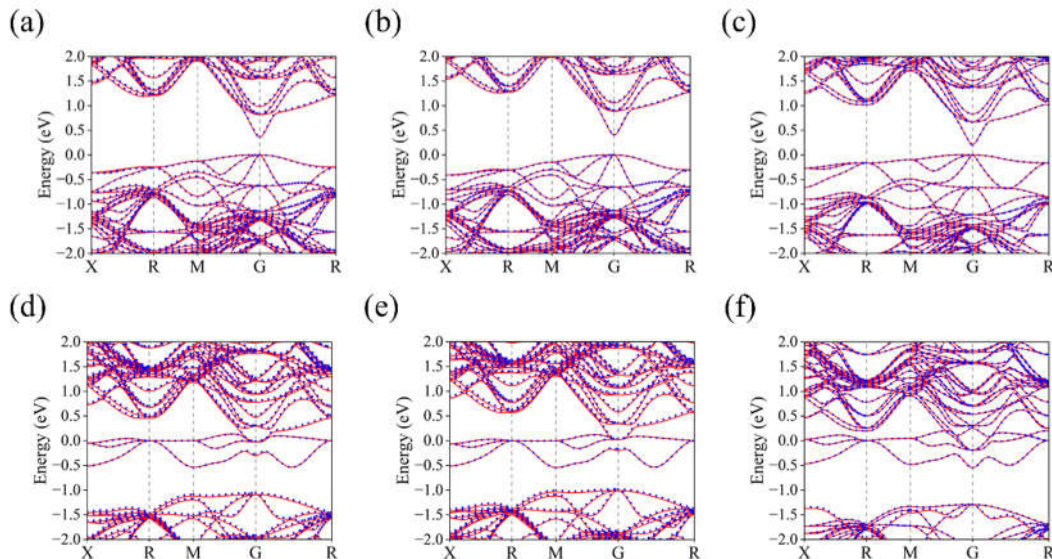


Fig.S3 The band structure for vacancy defects of GaAs computed by HamGNN-Q (red solid line) and DFT calculation (blue dotted line). (a) V_{Ga}^0 . (b) V_{Ga}^{3+} . (c) V_{Ga}^{3-} . (d) V_{As}^0 . (e) V_{As}^{3+} . (f) V_{As}^{3-} .

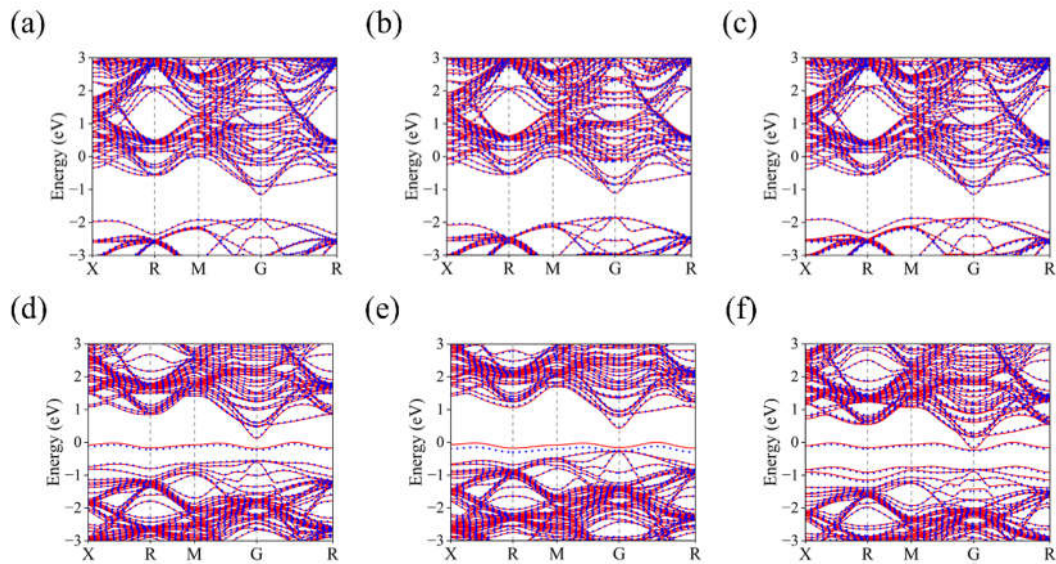


Fig.S4 The band structure for interstitial defects of GaAs computed by HamGNN-Q (red solid line) and DFT calculation (blue dotted line). (a) I_{Ga}^0 . (b) I_{Ga}^{3+} . (c) I_{Ga}^{3-} . (d) I_{As}^0 . (e) I_{As}^{3+} . (f) I_{As}^{3-} .

Testing for the band structure of defect clusters with different net charges

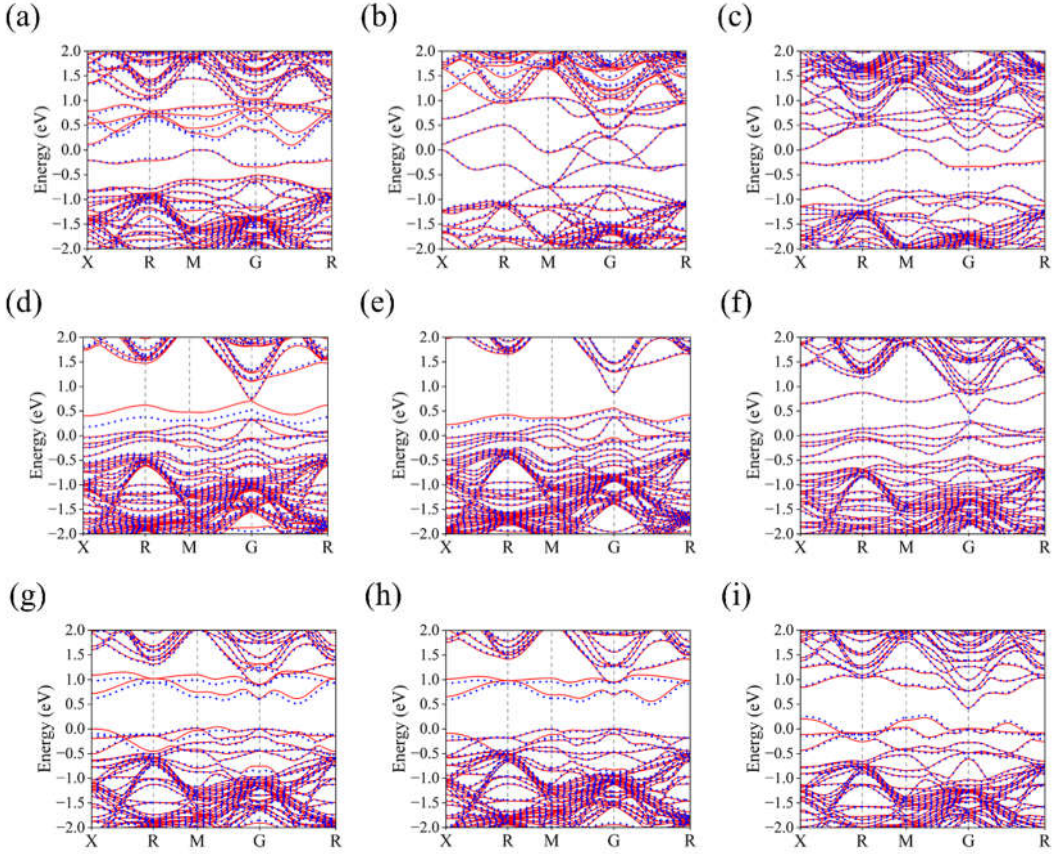


Fig.S5 The band structure for Defect clusters composed of vacancies of GaAs computed by HamGNN-Q (red solid line) and DFT calculation (blue dotted line). (a) DV_{As-As}^0 . (b) DV_{As-As}^{6+} . (c) DV_{As-As}^{6-} . (d) DV_{Ga-Ga}^0 . (e) DV_{Ga-Ga}^{6+} . (f) DV_{Ga-Ga}^{6-} . (g) DV_{As-Ga}^0 . (h) DV_{As-Ga}^{6+} . (i) DV_{As-Ga}^{6-} .

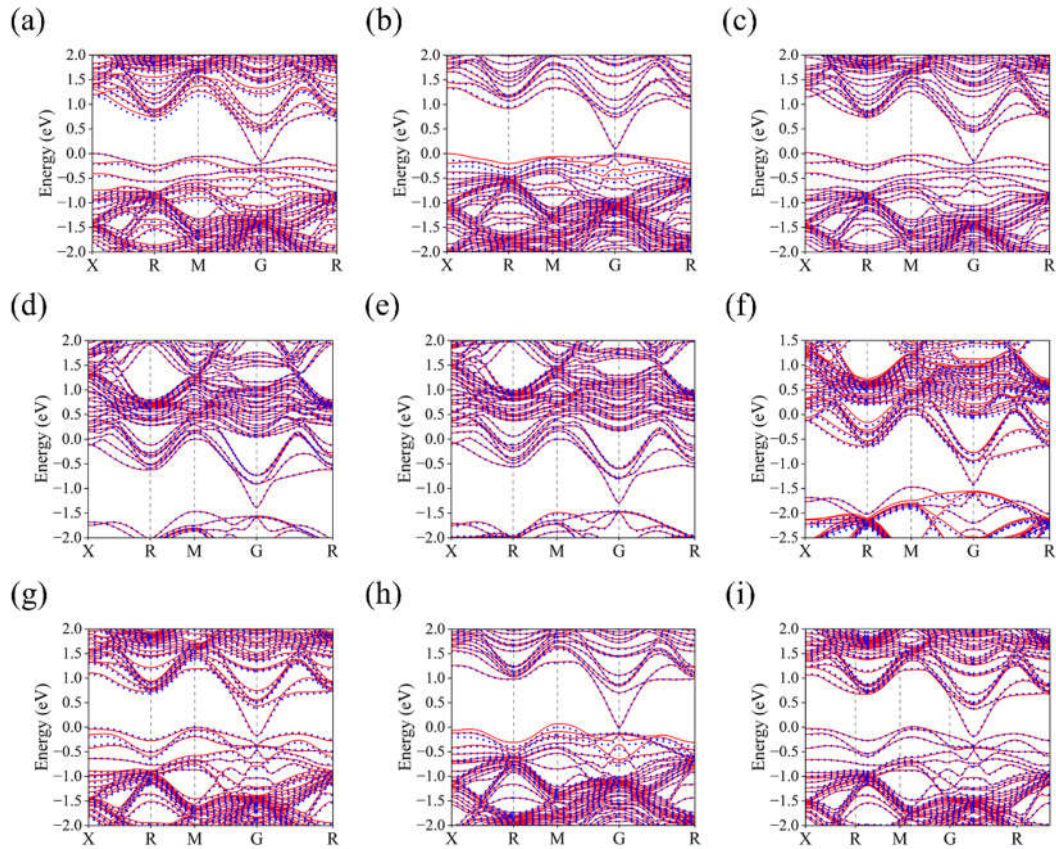


Fig.S6 The band structure for Defect clusters composed of interstitial atoms of GaAs computed by HamGNN-Q (red solid line) and DFT calculation (blue dotted line). (a) DI_{As-As}^0 . (b) DI_{As-As}^{6+} . (c) DI_{As-As}^{6-} . (d) DI_{Ga-Ga}^0 . (e) DI_{Ga-Ga}^{6+} . (f) DI_{Ga-Ga}^{6-} . (g) DI_{As-Ga}^0 . (h) DI_{As-Ga}^{6+} . (i) DI_{As-Ga}^{6-} .

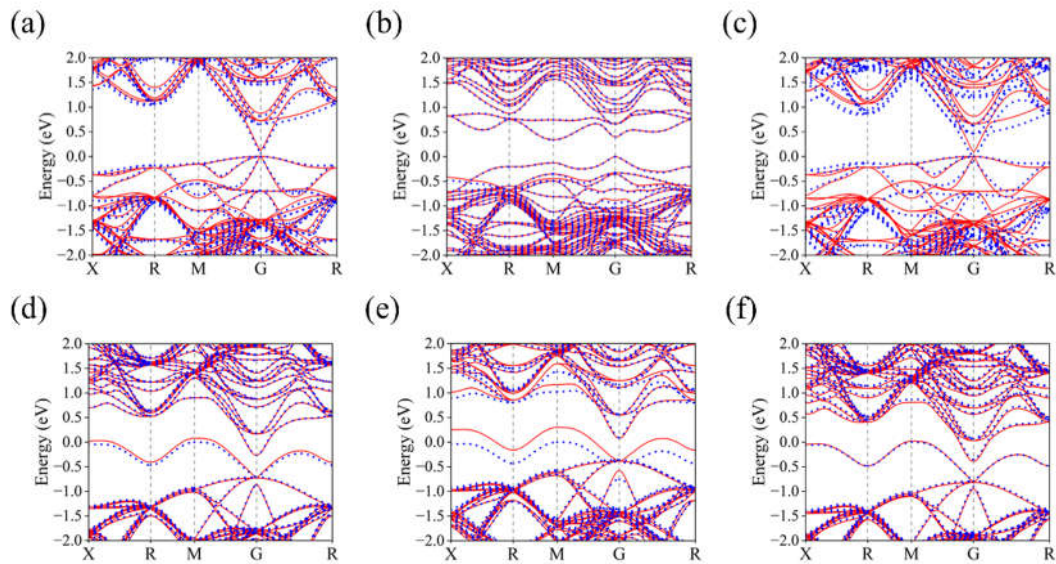


Fig.S7 The band structure for defect clusters composed of vacancies and interstitial atoms of GaAs computed by HamGNN-Q (red solid line) and DFT calculation (blue dotted line). (a) $[I_{Ga} - V_{As}]^0$. (b) $[I_{Ga} - V_{As}]^{6+}$. (c) $[I_{Ga} - V_{As}]^{6-}$. (d) $[I_{As} - V_{Ga}]^0$. (e) $[I_{As} - V_{Ga}]^{6+}$. (f) $[I_{As} - V_{Ga}]^{6-}$.

Testing the band structures of single-point defects with different net charges at various concentrations

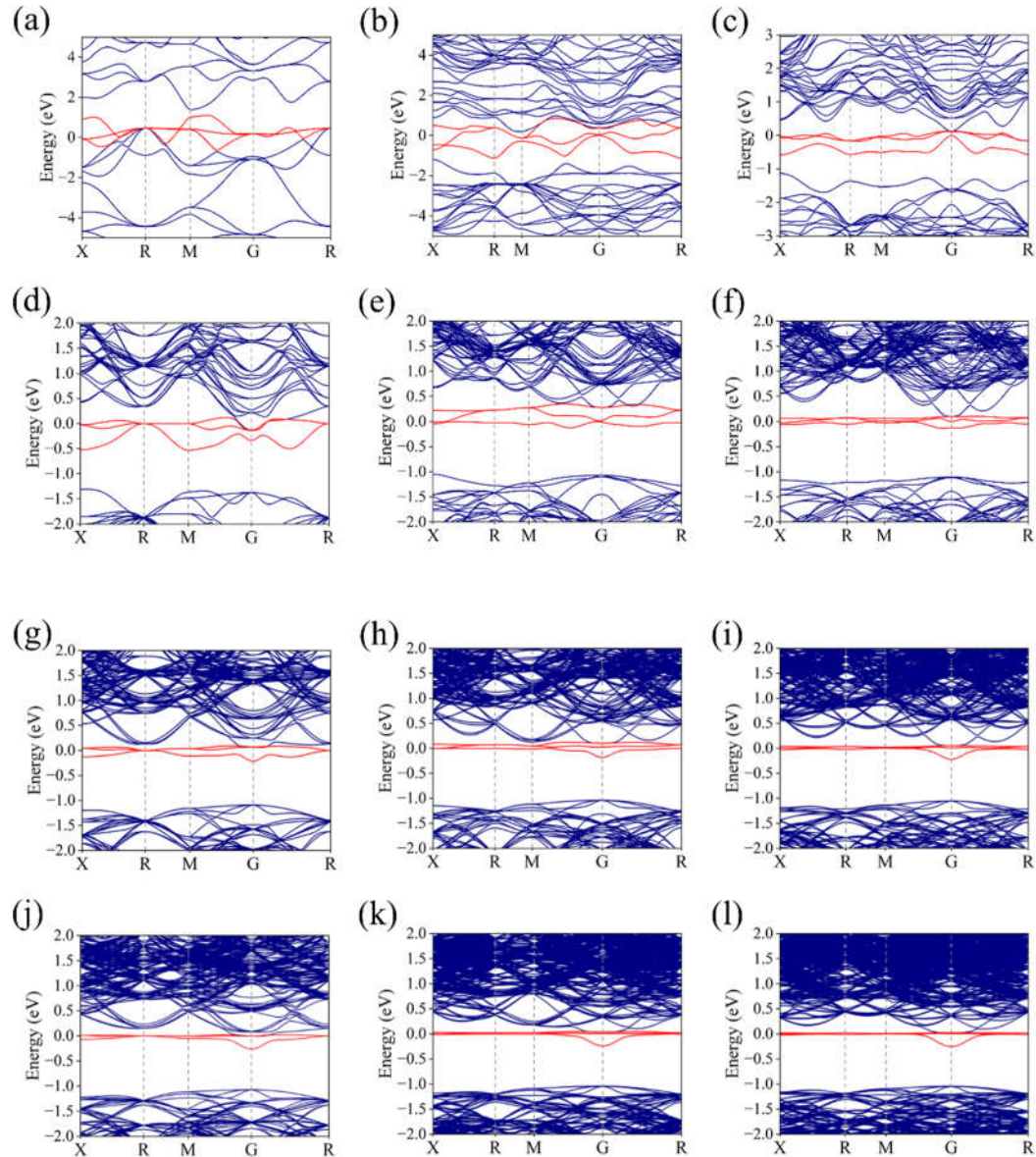


Fig.S8 (a)-(l) The band structure of the As vacancy defect with a charge amount of 0 ($q=0$) is depicted under various defect concentrations, namely 12.5 at. %, 6.25 at. %, 3.12 at. %, 1.56 at. %, 1.04 at. %, 0.70 at. %, 0.46 at. %, 0.35 at. %, 0.26 at. %, 0.20 at. %, 0.16 at. %, and 0.125 at. %, respectively.

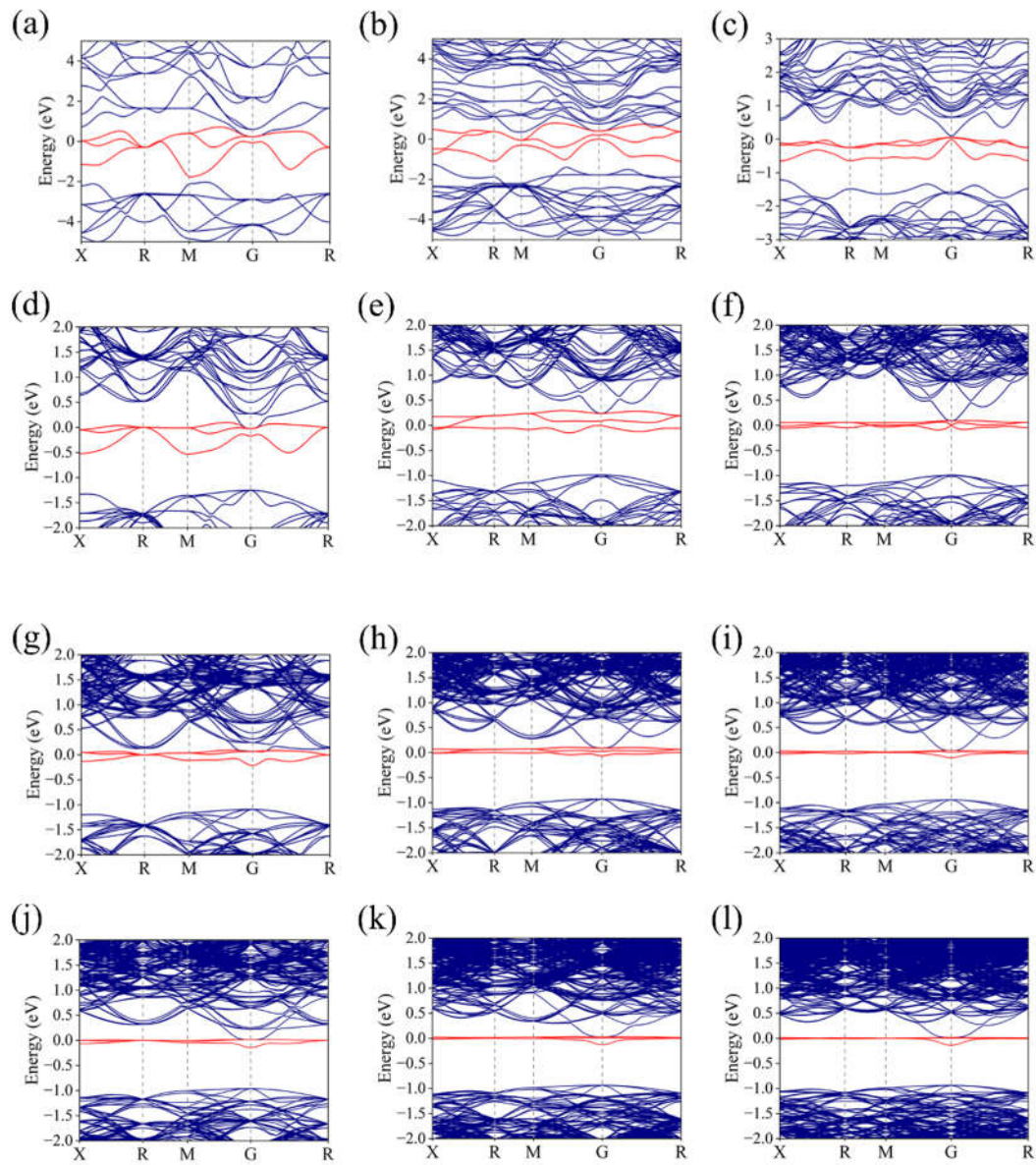


Fig.S9 (a)-(l) The band structure of As vacancy defects with a charge amount of 3 ($q=3$) is depicted under various defect concentrations, namely 12.5 at. %, 6.25 at. %, 3.12 at. %, 1.56 at. %, 1.04 at. %, 0.70 at. %, 0.46 at. %, 0.35 at. %, 0.26 at. %, 0.20 at. %, 0.16 at. %, and 0.125 at. %, respectively.

Testing for polarons induced by defects

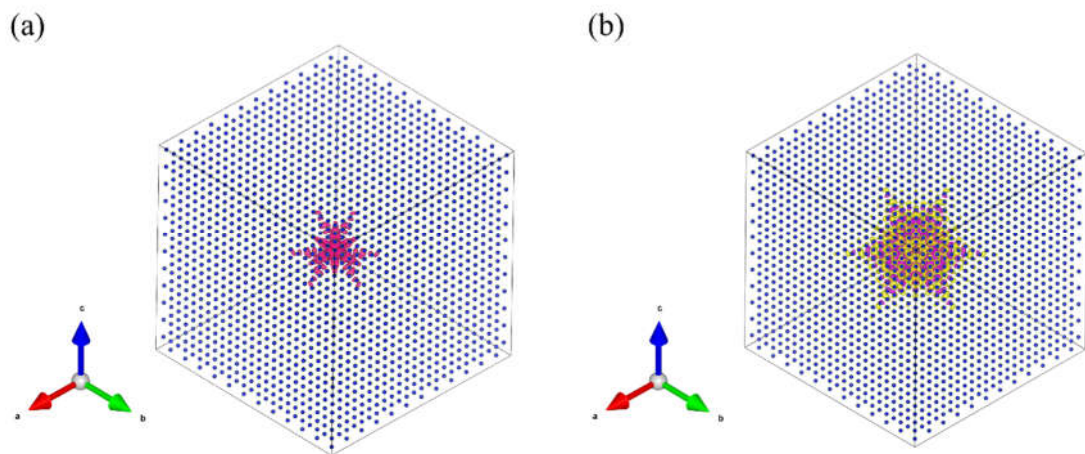


Fig.S10 The polarons induced by As_{Ga} substitution defects. (a) Charge density distribution of the polaron. (b) Wave function distribution of the polaron.

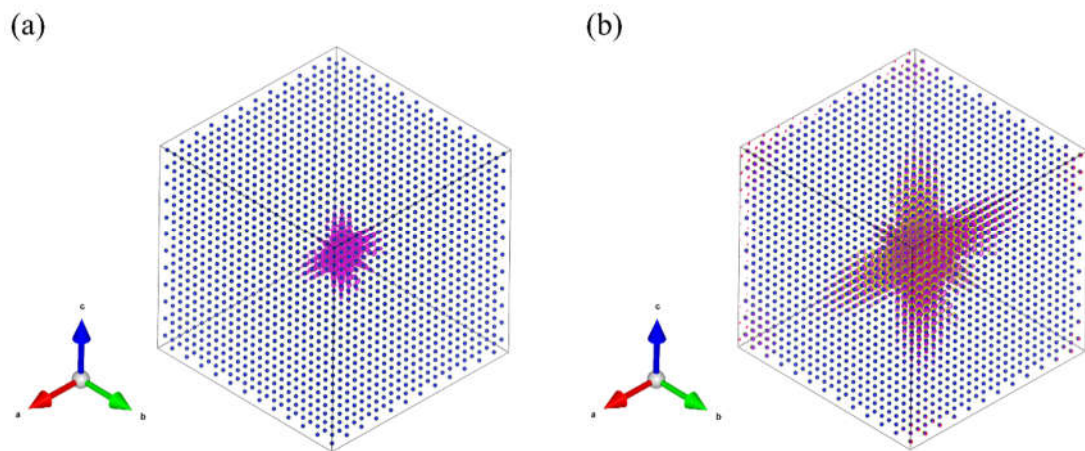


Fig.S11 The polarons induced by Ga_{As} substitution defects. (a) Charge density distribution of the polaron. (b) Wave function distribution of the polaron.

Prediction efficiency tests for the HamGNN-Q

To test the computational efficiency of our model, we tested it on supercells of various sizes. All prediction tests were performed using 64 CPU cores (Intel 9462). The result of prediction efficiency test is shown in the Table.S4.

Table.S4 Prediction efficiency tests for the HamGNN-Q model

Configuration	The number of atoms	Times(s)
$3 \times 3 \times 3$	216	44
$5 \times 5 \times 5$	1000	55
$8 \times 8 \times 8$	4096	91
$10 \times 10 \times 10$	8000	122
$12 \times 12 \times 12$	13824	217
$14 \times 14 \times 14$	21952	278

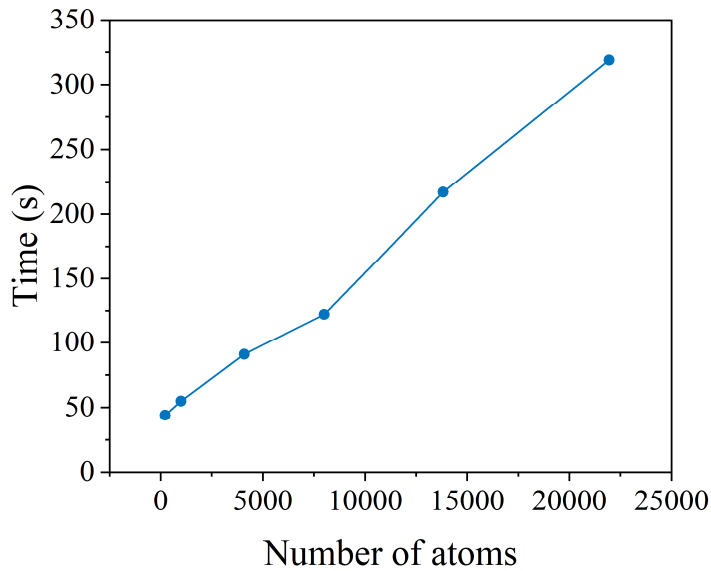


Fig.S12 Prediction efficiency of HamGNN-Q for various sizes of superlattice.

From Fig.S12, it can be observed that the prediction time increases linearly with the number of atoms, indicating that the time complexity of our model is $O(N)$.

Testing in TiO_2 charged defect system using HSE hybrid-functional method

We performed structural sampling via molecular dynamics, followed by HSE-based DFT calculations using the HONPAS¹¹ software package. These calculations were carried out for a $2\times 2\times 2$ supercell (48 atoms) with a $5\times 5\times 3$ Monkhorst–Pack k-point grid. The dataset consists of 800 samples and was divided into the training set, test set, and validation set in a ratio of 0.8:0.1:0.1.

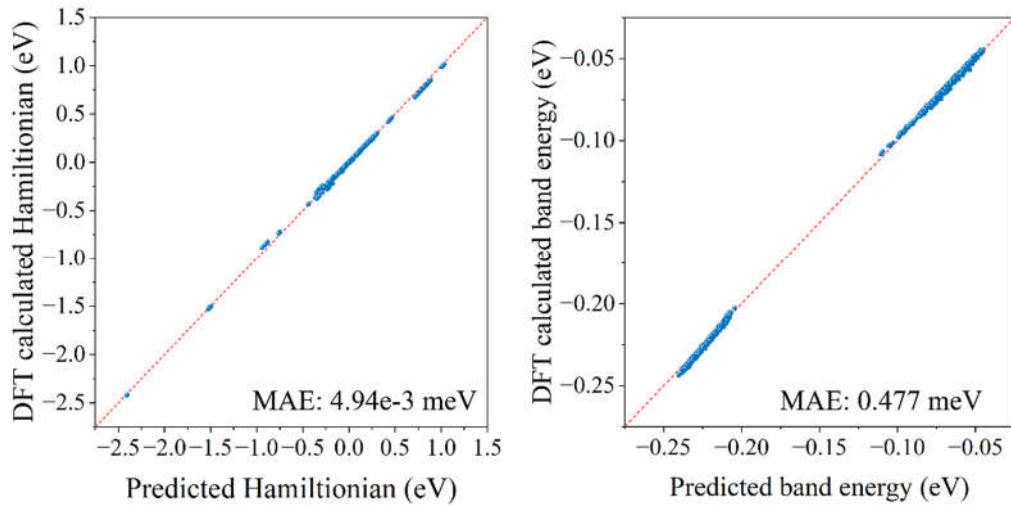


Fig.S13 (a) Comparison of HamGNN-Q predicted Hamiltonian matrix elements with HONPAS-calculated matrix elements on the test set. (b) Comparison of HamGNN-Q predicted and HONPAS calculated band energies on the test set.

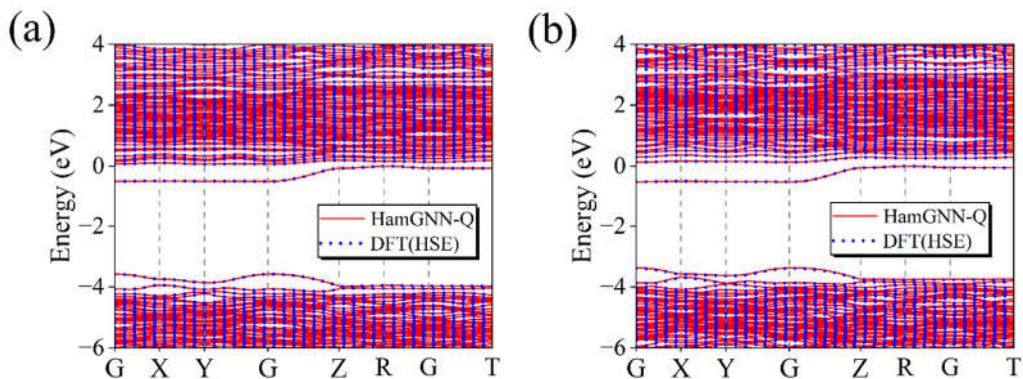


Fig.S14 (a) The band structure of the charged defective TiO_2 system is computed by HamGNN-Q (red solid line) and DFT calculation (blue dotted line). (a) V_O^0 (b) V_O^{2+} .

Reference

- ¹ G. Kresse, and J. Furthmüller, “Efficient iterative schemes for *ab initio* total-energy calculations using a plane-wave basis set,” Phys. Rev. B **54**(16), 11169–11186 (1996).
- ² P.E. Blöchl, “Projector augmented-wave method,” Phys. Rev. B **50**(24), 17953–17979 (1994).
- ³ G. Kresse, and D. Joubert, “From ultrasoft pseudopotentials to the projector augmented-wave method,” Phys. Rev. B **59**(3), 1758–1775 (1999).
- ⁴ J.P. Perdew, K. Burke, and M. Ernzerhof, “Generalized Gradient Approximation Made Simple,” Phys. Rev. Lett. **77**(18), 3865–3868 (1996).
- ⁵ T. Ozaki, “Variationally optimized atomic orbitals for large-scale electronic structures,” Phys. Rev. B **67**(15), 155108 (2003).
- ⁶ A. Musaelian, S. Batzner, A. Johansson, L. Sun, C.J. Owen, M. Kornbluth, and B. Kozinsky, “Learning local equivariant representations for large-scale atomistic dynamics,” Nat Commun **14**(1), 579 (2023).
- ⁷ A. Hjorth Larsen, J. Jørgen Mortensen, J. Blomqvist, I.E. Castelli, R. Christensen, M. Dułak, J. Friis, M.N. Groves, B. Hammer, C. Hargus, E.D. Hermes, P.C. Jennings, P. Bjerre Jensen, J. Kermode, J.R. Kitchin, E. Leonhard Kolsbjerg, J. Kubal, K. Kaasbjerg, S. Lysgaard, J. Bergmann Maronsson, T. Maxson, T. Olsen, L. Pastewka, A. Peterson, C. Rostgaard, J. Schiøtz, O. Schütt, M. Strange, K.S. Thygesen, T. Vegge, L. Vilhelmsen, M. Walter, Z. Zeng, and K.W. Jacobsen, “The atomic simulation environment—a Python library for working with atoms,” J. Phys.: Condens. Matter **29**(27), 273002 (2017).

⁸ A. Paszke, S. Gross, F. Massa, A. Lerer, J. Bradbury, G. Chanan, T. Killeen, Z. Lin, N. Gimelshein, L. Antiga, A. Desmaison, A. Köpf, E. Yang, Z. DeVito, M. Raison, A. Tejani, S. Chilamkurthy, B. Steiner, L. Fang, J. Bai, and S. Chintala, “PyTorch: An Imperative Style, High-Performance Deep Learning Library,” (2019).

⁹ S.P. Ong, W.D. Richards, A. Jain, G. Hautier, M. Kocher, S. Cholia, D. Gunter, V.L. Chevrier, K.A. Persson, and G. Ceder, “Python Materials Genomics (pymatgen): A robust, open-source python library for materials analysis,” Computational Materials Science **68**, 314–319 (2013).

¹⁰ M. Geiger, and T. Smidt, “e3nn: Euclidean Neural Networks,” (2022).

¹¹ X. Qin, H. Shang, H. Xiang, Z. Li, and J. Yang, “HONPAS : A linear scaling open-source solution for large system simulations,” Int J of Quantum Chemistry **115**(10), 647–655 (2015).